Ocean Engineering xxx (xxxx) xxx

Contents lists available at ScienceDirect

Ocean Engineering

journal homepage: www.elsevier.com/locate/oceaneng

Effect of wave inhomogeneity on fatigue damage of mooring lines of a side-anchored floating bridge

Jian Dai [a,*], Bernt Johan Leira [a], Torgeir Moan [a], Hagbart Skage Alsos [b]

[a] Department of Marine Technology, Norwegian University of Science and Technology, 7049, Trondheim, Norway
[b] SINTEF Ocean, 7052, Trondheim, Norway

ARTICLE INFO

Keywords:
Floating bridge
Mooring line
Wave inhomogeneity
Short-crested
Fatigue damage

ABSTRACT

Mooring systems are important structural components of very long floating bridges. They effectively limit the transverse motions of the bridge under environmental loads. They also add viscous hydrodynamic damping to the entire system. The safe and economical design of mooring systems is thus important but also challenging especially when the wave conditions are inhomogeneous. In this paper, a computational study is carried out to investigate the responses of the mooring lines for a 4.6 km long fjord crossing floating bridge accounting for inhomogeneous wave conditions. Based on the structural responses, this study also attempts to evaluate the fatigue damage in the mooring lines by using different fatigue analysis methods. The accuracy of the spectral methods is examined by comparison with the conventional rainflow cycle counting algorithm. Numerical studies are conducted to obtain an indication of the effect of various wave inhomogeneities on the fatigue damage in the mooring lines.

1. Introduction

Floating bridges are sophisticated structures across waterbodies subjected to complex loading conditions. They take advantage of the natural buoyancy to carry the gravity loads. They also face fewer complications arising from large water depths and/or soft seabed conditions that commonly hinder the adoption of bottom-founded structures for transportation purposes. Owing to these distinct advantages, floating bridges are recognised as a favourable and practical option in the E39 coastal highway project led by the Norwegian Public Road Administration (Statens vegvesen) to replace the time-consuming ferry trips across the wide and deep Norwegian fjords (COWI, 2019). However, the design and construction of a safe and cost-effective floating bridge could still be technically challenging, especially when the span is very long and the environmental conditions are complicated. Taking the Bjørnafjord in Norway as an example, the very long crossing of up to 5 km results in inevitably slender and flexible floating bridge designs, leading to significant hydroelastic responses of the bridge structure under wave actions (Cheng et al., 2018a; Kvåle et al., 2016; Viuff et al., 2018, 2019; Xiang and Løken, 2019; Xiang et al., 2018). In addition, the wave conditions are observed to be nonhomogeneous owing to the complex topology and the large span of the crossing (Cheng et al., 2019a). This introduces further complexities to the proper modelling and detailed study of the dynamic responses of the floating bridge (Cheng et al., 2018b; Dai et al., 2020a).

In an attempt to effectively limit the transverse motions and bending moments of the bridge structure under environmental loads, a design concept comprising a side-anchored floating pontoon bridge was proposed and is currently under feasibility investigations (DNV, 2018a; Multiconsult, 2017). Four clusters of mooring lines are attached to selected bridge pontoons spaced about 1 km apart. Besides limiting the transverse response, these mooring lines are also expected to add viscous hydrodynamic damping to the bridge structure. Therefore, the mooring lines play a vital role in the structural behaviour of the floating bridge under complicated environmental conditions and the safe and economical design of these structural components is of great importance. However, to the best knowledge of the authors, the effect of inhomogeneous wave conditions on the structural responses of the mooring systems for a very long floating bridge or similar slender marine structures has not been reported in the open literature.

Besides the structural responses, it is also important to examine the fatigue damage in the mooring lines due to the cyclic nature of the wave loads. A preliminary study on the current floating bridge design concept considering homogeneous wave conditions reveals that the safe design

* Corresponding author. Department of Marine Technology, Norwegian University of Science and Technology, Otto Nielsens veg 10, 7049, Trondheim, Norway.
E-mail address: jian.dai@ntnu.no (J. Dai).

https://doi.org/10.1016/j.oceaneng.2020.108304
Received 14 April 2020; Received in revised form 15 September 2020; Accepted 25 October 2020
Available online 28 October 2020

of some mooring lines may be governed by their fatigue life (Multiconsult, 2017). Unfortunately in the context of inhomogeneous wave conditions, the existing literature again lacks the information pertaining to the fatigue damage in the mooring lines for a very long floating bridge or similar structures. In a typical fatigue analysis, the conventional rainflow cycle counting method is commonly employed. Alternatively, spectral methods that are computationally efficient may be advantageous especially at the stages of design conceptualisation and initial feasibility studies when the structural configuration is subjected to iterative changes and optimisations. Commonly used spectral methods include the method by Dirlik (1985), the formula by Benasciutti and Tovo (2005), the bimodal method proposed by Jiao and Moan (1990) and the trimodal method by Gao and Moan (2008). These models were developed for Gaussian processes. When the processes are narrow-band, the classic Rayleigh model is applicable (Bouyssy et al., 1993; Gao and Moan, 2009; Miles, 1954). The comparison of various spectral fatigue analysis methods was made by several researchers (Benasciutti and Tovo, 2006; Chang et al., 2017; Han et al., 2020; Xu et al., 2014). Among these approaches, the Dirlik's method is found to perform quite well for both wide- and narrow-band Gaussian processes by comparison with the rainflow cycle counting method (Arany et al., 2014; Bouyssy et al., 1993; Yeter et al., 2016). This method has been extensively applied to the

(a)

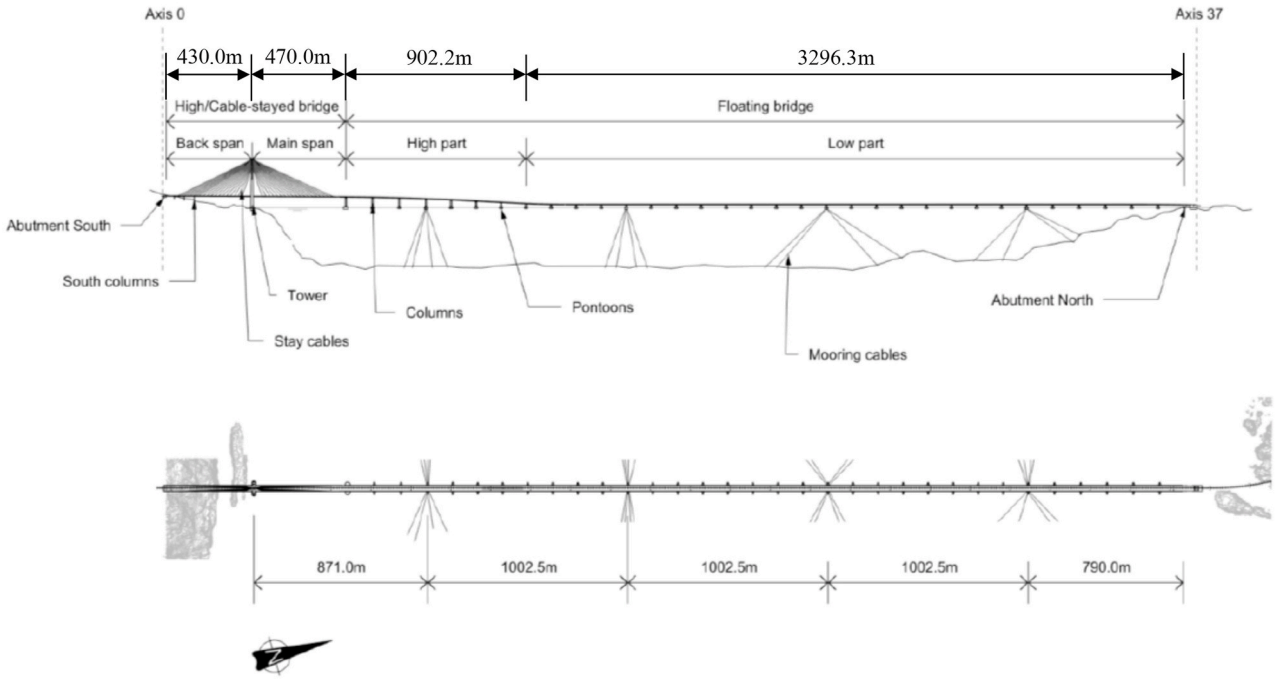

(b)

Fig. 1. Floating bridge design concept: (a) artistic impression and (b) side and plan views (Multiconsult, 2017).

fatigue analysis of marine structures including wind turbines and offshore platforms under the action of complex environmental loads (Arany et al., 2014; Bouyssy et al., 1993; Chaudhury and Dover, 1985; Chen and Basu, 2018; Gao and Moan, 2009; Yeter et al., 2015, 2016). Methods also exist for non-Gaussian processes due to nonlinear structural behaviour or non-Gaussian excitations (Chang et al., 2017; Gao and Moan, 2007; Winterstein, 1988). Thus, it is interesting to assess the applicability of the spectral methods such as Dirlik's method and the simple Rayleigh model for fatigue damage estimation of the mooring lines for a very long floating bridge under the action of inhomogeneous wave loads.

The focus of the present study is therefore twofold. First, we study the structural responses of the mooring lines for a 4.6 km long floating bridge under the action of inhomogeneous wave conditions. Next, the fatigue damage in the mooring lines is evaluated by using different fatigue analysis methods. The applicability of closed form expressions of the fatigue damage based on spectral parameters is examined, and the accuracy is tested by comparison with the conventional rainflow cycle counting algorithm. Numerical studies are carried out with the aim to obtain an indication of the effect of various wave inhomogeneities on the fatigue damage of mooring lines.

The remainder of the paper is organised as follows. Section 2 describes the numerical model for the time-domain response analysis of the floating bridge considering inhomogeneous wave loads. Section 3 examines the structural responses of the mooring lines. Section 4 investigates the various effects of wave inhomogeneity on the fatigue damage in the mooring lines. Finally, Section 5 concludes the findings of the study.

2. Numerical model and methodology

2.1. Floating bridge model

The current design concept for crossing of the Bjørnafjord features a straight and side-anchored floating bridge as shown in Fig. 1. The design concept comprises a cable-stayed bridge segment at the south end with a main span of 470 m and a back span of 430 m. The bridge deck is elevated 49 m above the mean sea level for navigation purposes. This cable-stayed bridge segment connects to the floating bridge segment which is composed of a 902.2 m long transitional high part and a 3296.3 m long low part. Pontoons spaced approximately 125 m apart are engaged in order to provide support to the floating bridge girder in the vertical direction. To effectively limit the transverse motion under environmental loads, the bridge is side-anchored by four evenly spaced clusters of mooring lines in addition to the bridge abutments at the two ends.

As the low part of the floating bridge constitutes the primary segment of the bridge design concept, an idealised numerical bridge model is therefore established by reasonably extending this low part to approximately the length of the entire crossing, as shown in Fig. 2. Besides, the geometric parameters are also regularised for the sake of simplification. For example, the spacing between two adjacent pontoons (labelled A1 to A35) is set to 125 m. In view of the fact that the varying topography has little effect on the wave excitation forces (Cheng et al., 2018a), a constant water depth of 300 m which represents approximately the average water depth along the crossing is adopted. Consequently, the four mooring clusters are standardised by employing an identical spread layout. Note that in each mooring cluster, a number of eight mooring lines are attached to the sidewall of the moored pontoon at 3 m draught with an identical pretension. The spread angles of line 1 to line 8 in each cluster are 75°, 80°, 100°, 105°, 255°, 260°, 280° and 285°, respectively, anticlockwise from the global *x*-axis. The mooring lines are for a relatively taut system based on a standard composition of a spiral strand segment with plastic sheathing of 11 mm thickness sandwiched by two studless chain segments of grade R4. Two different pretensions, namely 1500 kN and 1630 kN, are applied to the end clusters (clusters 1 and 4) and internal clusters (clusters 2 and 3), respectively. This is in order to match the transverse stiffness of the mooring clusters applied in the

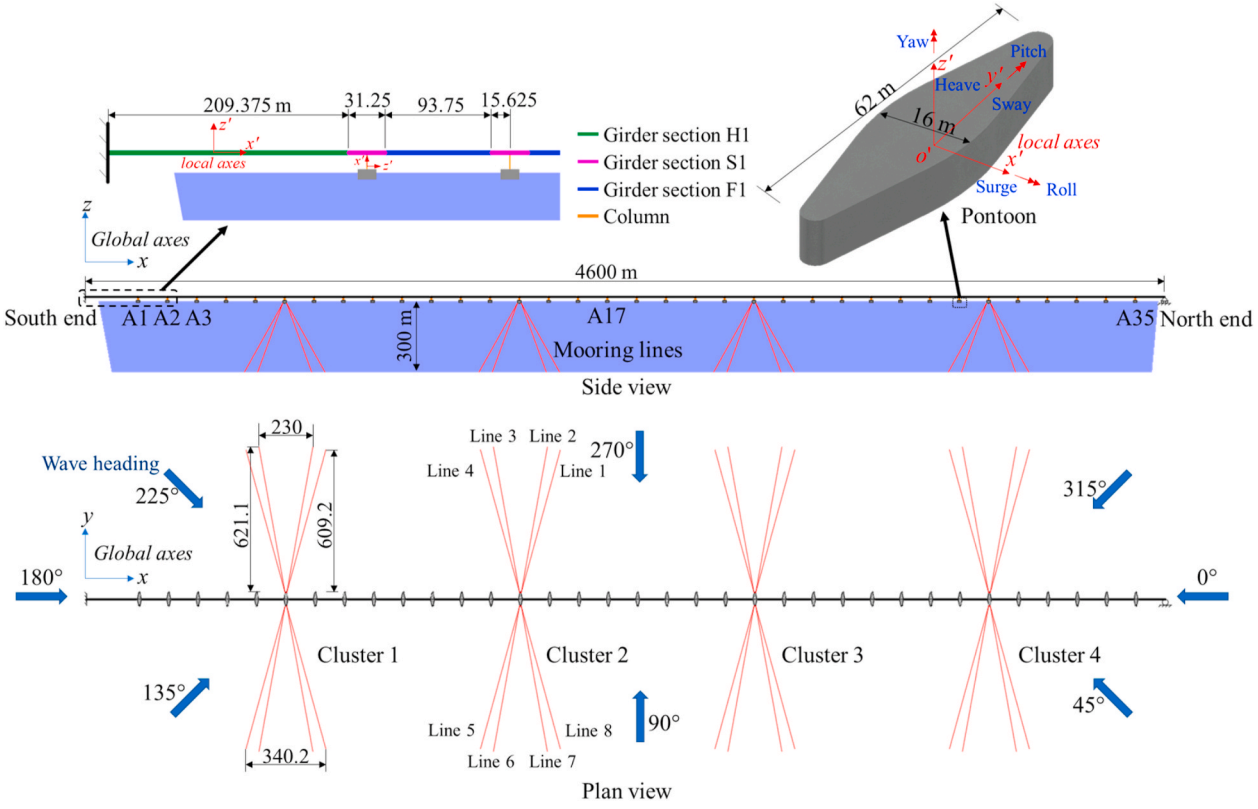

Fig. 2. Idealised floating bridge model.

design concept (Multiconsult, 2017). Fig. 3 shows the force-displacement curves of the mooring clusters subjected to the two different pretensions. Table 1 summarises the cross-sectional properties of the bridge girder and column. Table 2 lists the structural properties of the mooring lines. Note that the chain and wire segments were designed with different diameters to have the similar minimum breaking load of approximately 15,000 kN under corroded conditions (DNV, 2018a). The parameters for the chain segments are based on Vicinay's product catalogue (Vicinay, 2020), whereas the parameters for the wire segments are based on Bridon's product catalogue (Calverley, 2004). The pontoon properties are given in Table 3. The boundary conditions are as follows: all six degrees of freedom are fully restrained at the bridge south end, while the translation along the x-axis and rotation about the z-axis are allowed at the north end. Note that all the abovementioned parameters are adopted according to the design concept of the floating bridge (DNV, 2018a; Multiconsult, 2017). Also note that near the south end, the length of the first span is purposely chosen to match the dynamic properties of the cable-stayed bridge segment.

In the numerical model, the bridge pontoons are treated as rigid bodies subjected to wave loads. The hydrodynamic coefficients, i.e. the added mass and potential damping properties, and the wave excitation force transfer functions corresponding to the bridge pontoons are evaluated in the frequency domain by using the commercial tool WAMIT (WAMIT, 2019). Fig. 4 shows an example of the panel models of the wet surface of two typical pontoons constructed for use in WAMIT. In view of the fact that the pontoon spacing is relatively large when compared with the length of the wind waves in the fjord (Statens vegvesen, 2018), the effect of hydrodynamical coupling between pontoons is expected to be small and thus not accounted for. Then, the governing equations of motion for the bridge pontoons in the time domain can be obtained in accordance with Cummins theory (Cummins, 1962) as

Table 1
Structural properties of bridge girder and column sections. ρA is the mass per unit length. $r_{x'}$ refers to the radius of gyration about the local x'-axis. EA denotes axial stiffness. $EI_{y'}$ and $EI_{z'}$ are the flexural rigidity about the local axes. GJ is the torsional stiffness.

Section	ρA (kg/m)	$r_{x'}$ (m)	EA (kN)	$EI_{y'}$ (kNm^2)	$EI_{z'}$ (kNm^2)	GJ (kNm^2/rad)
Girder H1	17,530	8.3	2.9×10^8	6.0×10^8	2.3×10^{10}	4.7×10^8
Girder S1	19,780	8.1	3.5×10^8	8.5×10^8	2.4×10^{10}	6.4×10^8
Girder F1	16,040	8.2	2.5×10^8	6.7×10^8	1.9×10^{10}	5.4×10^8
Column	9,180	5.0	3.2×10^8	3.1×10^9	2.0×10^9	2.7×10^9

Table 2
Structural properties of mooring lines.

Segment	Nominal diameter (mm)	Length (m)	ρA (kg/m)	EA (kN)
Top chain	147	50	432.2	1.73×10^6
Wire	124	600	80.3	1.42×10^6
Bottom chain	147	50	432.2	1.73×10^6

$$\left(M_p + A_p^{\infty}\right)\ddot{u}_p(t) + \int_{-\infty}^{\infty} K_r(t-\tau)\dot{u}_p(\tau)d\tau + (K_b + K_h)u_p(t) = F_1^{exc}(t) + F_2^{exc}(t), \tag{1}$$

where $\mathbf{M}_p$ refers to the pontoon's structural mass matrix, $\mathbf{A}_p^{\infty}$ denotes the matrix of added mass at infinite frequency, $\mathbf{K}_r(t-\tau)$is the retardation function which represents the fluid's memory effect, $\mathbf{K}_b$ is a structural

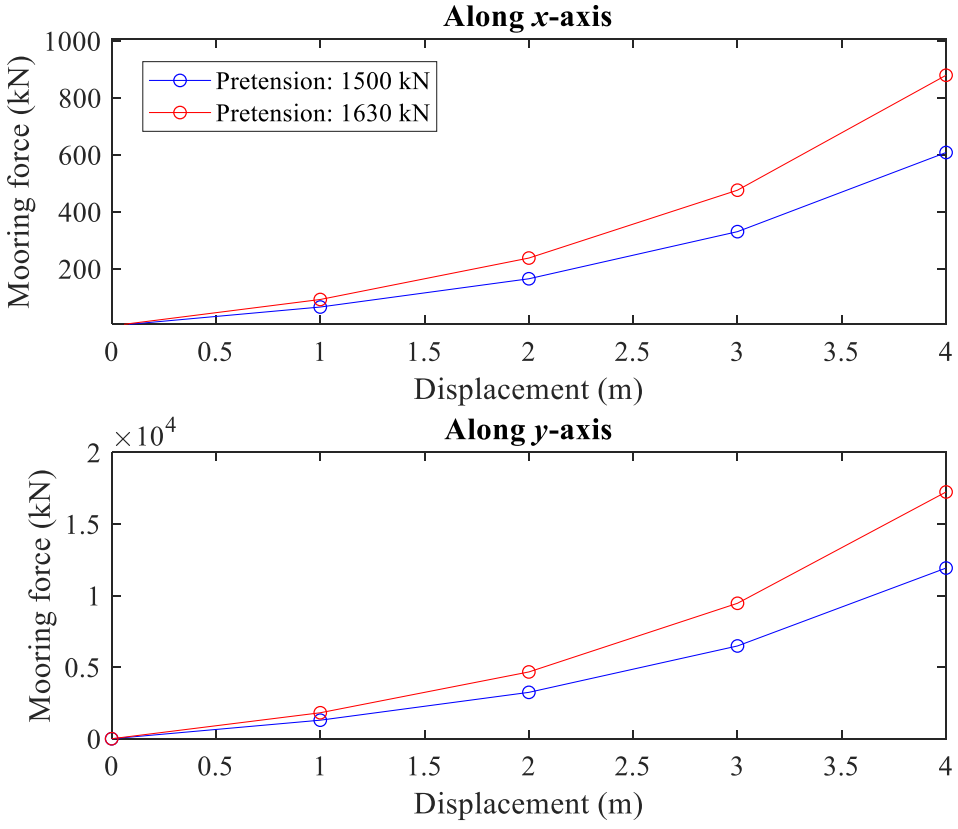

Fig. 3. Restoring curves of mooring clusters.

Table 3
Pontoon properties.

Property	Moored pontoon	Unmoored pontoon
Weight (ton)	1452	850
Displacement (m3)	5.7×10^3	3.3×10^3
Roll inertia (ton m^2)	4.2×10^5	2.2×10^5
Pitch inertia (ton m^2)	6.1×10^4	2.3×10^4
Yaw inertia (ton m^2)	4.2×10^5	2.3×10^5
Heave stiffness (kN/m)	6.7×10^3	6.7×10^3
Roll stiffness (kNm/rad)	1.5×10^6	1.5×10^6
Pitch stiffness (kNm/rad)	8.9×10^4	8.9×10^4

stiffness matrix that represents the restraining effect of the bridge, $\mathbf{K}_h$ is the hydrostatic restoring stiffness matrix, $\mathbf{u}_p$ is the displacement vector of the pontoon, $\mathbf{F}_1^{exc}(t)$ is the force vector containing the first order wave excitation load components, and correspondingly, $\mathbf{F}_2^{exc}(t)$ is the force vector containing the second order difference-frequency wave excitation load components.

The other structural components, namely the girders, columns and mooring lines, are modelled by means of the finite element method. In view of their slenderness, the girders and columns are represented by using Euler-Bernoulli beam elements, while the mooring lines are discretised into bar elements considering their geometric stiffness. Besides their self-weight, the hydrodynamic loads acting on the mooring lines are considered according to the Morison equation as

$$f_m = \rho_w V \dot{u}_w + \rho_w C_a V\left(\dot{u}_w - \dot{u}_m\right) + \frac{1}{2}\rho_w C_d D(u_w - u_m)|u_w - u_m|, \tag{2}$$

where ρ_w denotes the density of seawater, V is the volume per unit length of the mooring line, D is the diameter of the mooring line, $C_a = 1.0$ is the added mass coefficient, and C_d is the quadratic drag coefficient. Note that C_d in the transverse direction is taken as 2.4 for the top and bottom chain segments, while it is set to 1.2 for the intermediate wire segments; for the longitudinal direction, C_d is taken as 1.15 and 0.1, respectively (Multiconsult, 2017). u_w denotes the flow velocity, and u_m is the corresponding velocity of the submerged mooring line.

By assemblage, the governing equations of motion for the entire floating bridge model in the global coordinate system may be expressed in a compact matrix form as

$$M_B\ddot{u}_B + C_B\dot{u}_B + \int_{-\infty}^{\infty} K_R(t-\tau)\dot{u}_B(\tau)d\tau + K_B u_B = F_B, \tag{3}$$

where $\mathbf{M}_B$ denotes the global mass matrix of the entire floating bridge model, $\mathbf{C}_B$, is the global damping matrix, $\mathbf{K}_B$ is the global stiffness matrix, $\mathbf{F}_B$ is the global external load vector, $\mathbf{K}_R$ is the global matrix containing retardation functions for the degrees of freedom of the pontoons only, and $\mathbf{u}_B$ is the global displacement vector. Note that the superscript dots denote partial derivatives with respect to the time t.

Note that the global mass matrix $\mathbf{M}_B$ contains both the structural mass and the hydrodynamic added mass. Likewise, $\mathbf{C}_B$ comprises the contributions from the structural damping and the quadratic damping. For the modelling of the structural damping, the Rayleigh damping is adopted with a mass proportional coefficient of 0.001 and a stiffness proportional coefficient of 0.025. This results in a 0.5% damping ratio for the two lowest modes, which complies with the requirement stated in the design basis for steel structures (Statens vegvesen, 2018). The global stiffness matrix $\mathbf{K}_B$ contains the bridge structural stiffness and the hydrostatic restoring stiffness. The external load vector $\mathbf{F}_B$ includes the gravitational forces, buoyancy forces and wave excitation forces.

The commercial software package SIMA is employed for the numerical simulation of the floating bridge model through a coupled SIMO-RIFLEX task (SINTEF Ocean, 2019a; SINTEF Ocean, 2019b). Fig. 5 presents the first five vibration modes of the floating bridge. As it can be seen, all these modes correspond to the transverse vibration of the bridge girder and they possess long natural periods that may be excited by the slow varying second order difference-frequency wave load components. These vibration modes are also found to be coupled with the torsional modes of the bridge girder as a result of the restraining effect of the mooring lines. The lowest axial mode occurs at 11 s. As for the vertical vibration modes, they are found to be densely clustered near 7 s, which is close to the local wind-driven wave periods (Statens vegvesen, 2018). Therefore, the vertical motion and bending moment of the floating bridge are expected to be excited by the first order wave load components in a wind sea. More detailed information about the modal properties of the side-anchored floating bridge was reported by Dai et al. (2020a).

2.2. Inhomogeneous wave conditions

The combination of varying fjord topography and a very large span of up to 5 km has led to complicated wave conditions at the Bjørnafjord crossing. To characterise the local wave field, three Datawell Wave Riders (DWRs) were deployed along the planned bridge crossing to monitor the wave conditions at their respective locations. These three DWRs are close to the pontoons A4, A13 and A27, respectively. Field monitoring results reveal that the wave field across the Bjørnafjord is inhomogeneous (Cheng et al., 2019a). However, the coherence between the DWRs is found to be rather low as the distance between them is more than 1300 m. Nevertheless, the inhomogeneous wave field along the full length of the bridge span may still be reasonably modelled by assuming that: (1) the wave field surrounding any bridge pontoon is homogeneous (Ding et al., 2019; Wei et al., 2017, 2018), and (2) the spatial variation of wave characteristics (e.g. significant wave height H_s, peak period T_p and principal wave direction θ_p) across the pontoons between the DWRs is linear (Cheng et al., 2018b; Dai et al., 2020a).

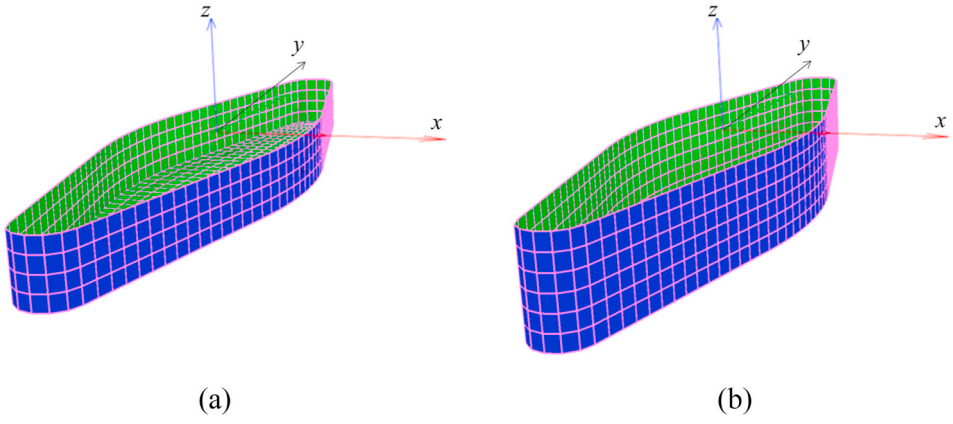

Fig. 4. Panel models of (a) unmoored pontoon and (b) moored pontoon.

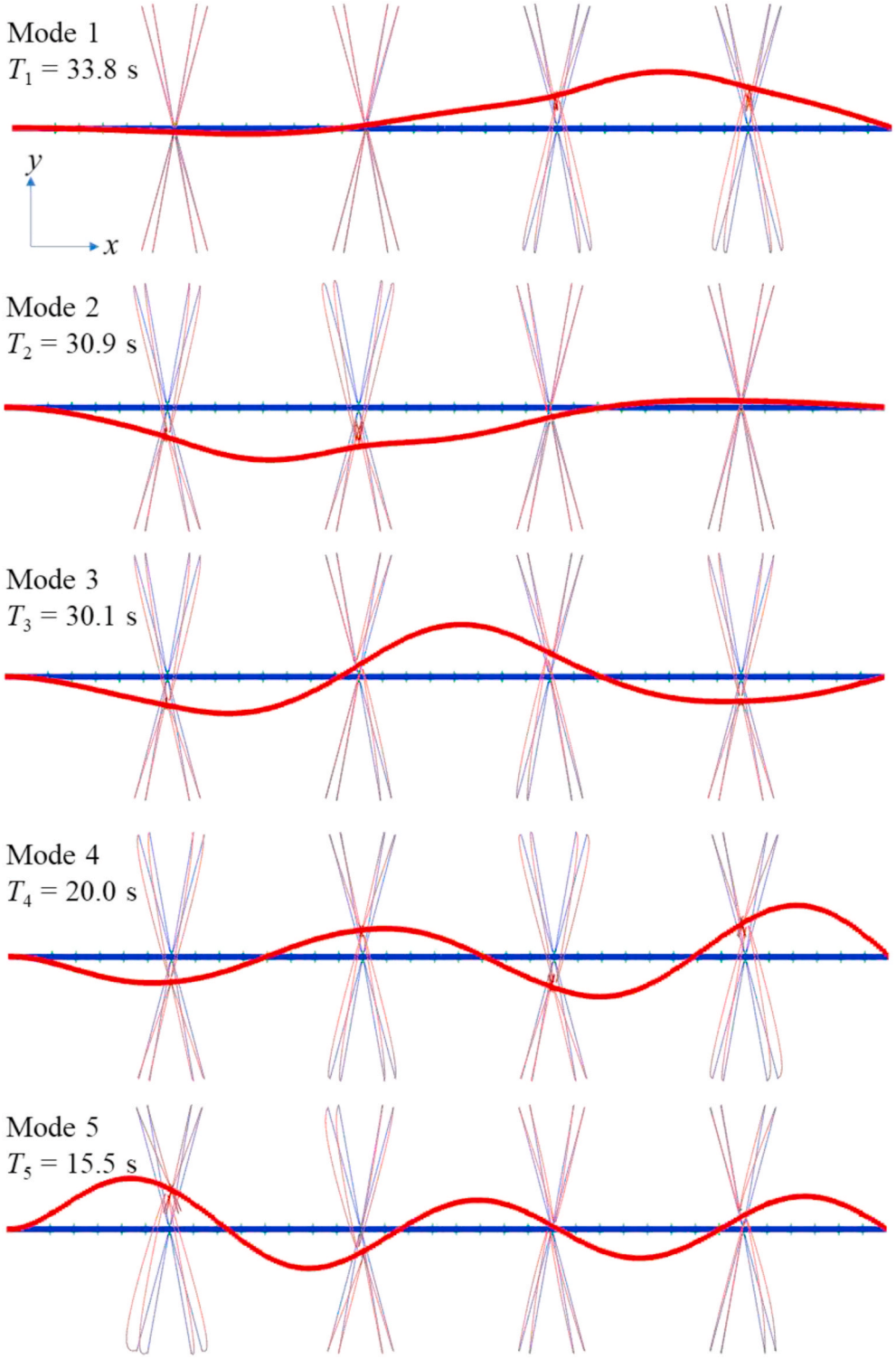

Fig. 5. Plan view of the first five eigen modes of the floating bridge model (blue lines refer to the undeformed bridge and red lines refer to the mode shape). (For interpretation of the references to colour in this figure legend, the reader is referred to the Web version of this article.)

With reference to the design basis for the crossing of the Bjørnafjord, the local wind-driven waves are short-crested and they may be described by using the JONSWAP spectrum (Statens vegvesen, 2018). Consequently, the directional spectrum $S_\zeta^j(\omega,\theta)$ characterising the wave conditions near an arbitrary bridge pontoon Aj, where j is an integer between 1 and 35, may be expressed as

$$S_\zeta^j(\omega,\theta) = S_\zeta^j(\omega) D_\zeta^j(\theta), \tag{4}$$

$$S_\zeta(\omega) = \frac{5}{16} A_\gamma H_s^2 \frac{\omega_p^4}{\omega^5} e^{-\frac{5}{4}\left(\frac{\omega}{\omega_p}\right)^{-4}} \gamma^{e^{-\frac{1}{2}\left(\frac{\omega-\omega_p}{\sigma\omega_p}\right)^2}}, \tag{5}$$

$$D_\zeta(\theta) = \frac{\Gamma\left(1+\frac{n}{2}\right)}{\sqrt{\pi}\Gamma\left(\frac{1}{2}+\frac{n}{2}\right)} \cos^n\left(\theta-\theta_p\right), \tag{6}$$

where $S_\zeta^j(\omega)$ denotes the unidirectional wave spectrum, and $D_\zeta^j(\theta)$ refers to the directional spreading function. $A_\gamma = 1 - 0.287\ln(\gamma)$, where $\gamma = 3.3$ is the non-dimensional peak shape parameter. $\omega_p = 2\pi/T_p$ is the peak angular frequency, and σ is the spectrum width parameter which equals 0.07 for $\omega \leq \omega_p$ and 0.09 for $\omega > \omega_p$. n is the spreading coefficient. For the locally short-crested wind waves in the Bjørnafjord, n may be taken as 4 (Statens vegvesen, 2018).

Fig. 6 shows the spatial variation of the significant wave height H_s, peak period T_p and principal wave direction θ_p corresponding to the 1-year homogeneous and inhomogeneous wave conditions at the Bjørnafjord. Note that the 1-year homogeneous wave condition is chosen according to the design basis (Statens vegvesen, 2018). Two different inhomogeneous wave conditions are considered.

The inhomogeneous wave condition 1 is established by first scaling the harshest wave condition with the highest H_s measured by the DWRs, which occurs at A27, to match the selected homogeneous wave condition, i.e. $H_s = 1.3$ m, $T_p = 4.6$ s and $\theta_p = 288°$. This is in line with the common practice in an engineering design in which the most severe sea state is often applied to the entire length of the structure. Correspondingly, the wave conditions measured by the other two DWRs at A4 and A13 are also adjusted with the same scaling factor. Then, a linear interpolation is employed to describe the wave conditions at other pontoon locations.

Besides, a different type of wave inhomogeneity is considered in this study. The inhomogeneous wave condition 2 described in Fig. 6 is adapted based on the wave inhomogeneity at the Sulafjord (Lei et al., 2016). It should be noted that the reported wave conditions at the Sulafjord are much harsher. In order to suit the wave conditions at the Bjørnafjord, the inhomogeneous wave condition at the Sulafjord is scaled down in order to match the worst wave condition with the selected homogeneous wave condition. This is in line with the treatment for the inhomogeneous wave condition 1.

Essentially, the inhomogeneous wave condition 1 is characterised by a spatial variation of θ_p. The inhomogeneity in H_s is small and T_p remains unchanged throughout the entire bridge length. As a contrast, the inhomogeneous wave condition 2 represents a significant spatial variation of H_s and T_p, while there is no change in θ_p across the bridge span.

In addition to the abovementioned parameters characterising the directional wave spectra at individual pontoon locations, the coherence and correlation between these wave spectra are also important. In a time domain simulation, this is represented by the random phase angles of the wave components in irregular seas. Due to the lack of information, only two conditions pertaining to the wave correlation are considered. The first condition refers to a fully coherent and correlated sea state where the random phase angles of each wave component are identical at all pontoon locations. Essentially, this describes a fully continuous wave field. The second condition refers to uncorrelated waves at different pontoons locations by assigning different random phase angles for various pontoon locations. Under such a circumstance, the waves along the bridge length are completely independent and random.

In this study, the following six wave load cases are considered in

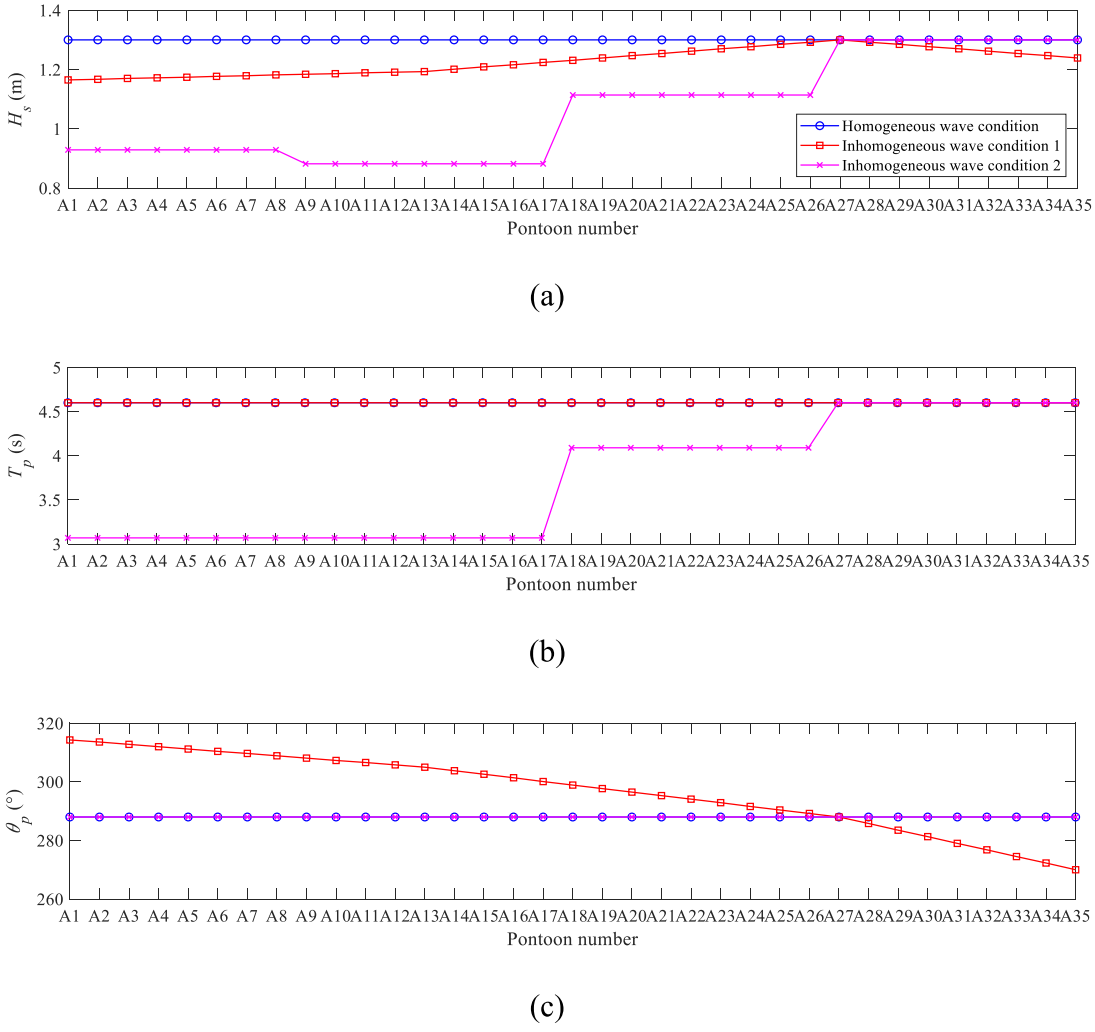

Fig. 6. 1-year homogeneous and inhomogeneous wave conditions: (a) H_s, (b) T_p and (c) θ_p.

order to investigate the effect of wave inhomogeneity on the mooring lines.

Load case 1 (LC1) describes the homogeneous wave condition with $H_s = 1.3$ m, $T_p = 4.6$ s and $\theta_p = 288^\circ$ for the entire crossing. The sea states along the bridge length are fully coherent and correlated.

Load case 2 (LC2) describes an inhomogeneous wave condition with constant $H_s = 1.3$ m, $T_p = 4.6$ s and $\theta_p = 288^\circ$ throughout the whole bridge length. However, the waves at different pontoon locations are completely uncorrelated by application of independent phase angles of wave components.

Load case 3.1 (LC3.1) describes the inhomogeneous wave condition 1 with varying significant wave height H_s and principal wave direction θ_p as shown in Fig. 6. The waves along the bridge length are fully coherent and correlated.

Load case 3.2 (LC3.2) describes the inhomogeneous wave condition 2 with varying significant wave height H_s and wave peak period T_p as shown in Fig. 6. Similar to LC3.1, the waves are fully coherent and correlated.

Load case 4.1 (LC4.1) describes the inhomogeneous wave condition 1 with varying wave characteristics (H_s and θ_p) as shown in Fig. 6, but the waves at different pontoon locations are completely uncorrelated.

Similarly, load case 4.2 (LC4.2) describes the inhomogeneous wave condition 2 with varying wave characteristics (H_s and T_p) as shown in Fig. 6, but the waves at different pontoon locations are completely uncorrelated.

It should be mentioned that the 1-year wave conditions are considered in this study due to the lack of available information regarding the long-term variation of inhomogeneous waves at the Bjørnafjord. The analysis of the long-term joint distribution of the environmental "intensity parameters" based on hindcast data shows that the wave periods of the selected wave conditions are fairly large (Cheng et al., 2019b). Furthermore, the information about the inhomogeneous wave 1 was based on field measurements over 1 year (Cheng et al., 2019a). Thus, it may be reasonable to employ the abovementioned wave conditions as representative annual maximum sea states for evaluating the structural responses of mooring lines due to the wave inhomogeneity. The fatigue analysis presented in this paper is solely for the purpose of obtaining an indication of the inhomogeneous wave effect on the fatigue damage, in view of the fact that comprehensive fatigue analysis depends on all possible wave conditions throughout the service life of the structure.

2.3. Numerical simulation

The simulations are conducted in the time domain and the Newmark constant acceleration scheme is adopted for solving the differential equations. To ensure the convergence of the results, the time interval Δt may be determined according to the following condition

$$\Delta t \leq \frac{T_{\min}}{20}, \tag{7}$$

where $T_{\min}$ refers to the smallest natural period of the floating bridge model that is of interest. In view of the fact that the energy of the local waves with $T \leq 2$ s is generally small (Statens vegvesen, 2018) and they are far away from the lowest vibration modes of the floating bridge, their effect on the dynamic responses of the bridge is expected to be insignificant. As a result, it is reasonable to adopt a time step size that is not exceeding 0.1 s.

For each of the abovementioned six wave load cases, five independent wave realisations are employed to bring down the stochastic uncertainties in the results. Each simulation has a length of 4500 s, in which the results for the initial 900 s contain transient responses and thus not used for the subsequent data analysis. The statistical values and power spectra presented in the following sections are based on the average of the five independent simulations for each wave load case.

As the focus of the study is on the inhomogeneous wave effect, other environmental effects such as wind and current as well as traffic loads are excluded. It should be highlighted that wind loads may have a considerable contribution to the low-frequency responses of the mooring lines. For fatigue analysis, it may be more appropriate to consider concurrent environmental loads in time domain simulations. Nevertheless, simplified methods exist for combining the fatigue damage from different load effect processes (Han et al., 2016, 2020; Huang and Moan, 2006; Lotsberg, 2005; Van Der Tempel, 2006). Besides, steady wind and current loads have an effect on the mooring tension which may alter the mooring stiffness and thus the stress ranges due to wave loads. The results from separate studies indicate that the maximum transverse displacements (along y-axis) at moored pontoons induced by 1-year steady environmental loads and wave loads are less than 1 m and 0.5 m, respectively (Dai et al., 2020b; Multiconsult, 2017). Within the relatively small range of displacement, the stiffness of the mooring clusters is virtually constant (see Fig. 3), thereby implying that the effect of neglecting steady wind and current loads on the fatigue damage of mooring lines is quite limited.

2.4. Fatigue analysis methods

It is commonly accepted that the rainflow cycle counting method predicts the fatigue damage most accurately when compared with its alternatives. In this method, a variable-amplitude cyclic stress time series is first decomposed into individual stress cycles s_i. It is assumed that these stress cycles s_i may be superimposed upon one another. Then, the accumulated fatigue damage D_f can be computed according to the Palmgren-Miner sum as

$$D_f = \sum_{i=1}^{n} \frac{n_i}{C} s_i^m, \tag{8}$$

where n_i is the number of cycles counted for stress range s_i, and C and m are the material parameters characterising the S–N curve of the material. For studless chain segments considered in this study, these material parameters are taken as $C = 6 \times 10^{10}$ and $m = 3$, respectively (DNV, 2018b). For the wire segments, $C = 1.7 \times 10^{17}$ and $m = 4.8$ (DNV, 2018b).

Instead of decomposing a cyclic stress time series into individual stress cycles as used in the rainflow cycle counting algorithm, Dirlik proposed a spectral approach to estimate the probability density function (PDF) of stress ranges s directly from the power spectrum of the time series (Dirlik, 1985). The PDF is expressed in terms of an exponential term and two Rayleigh terms as

$$P(s) = \frac{\frac{G_1}{Q} e^{-\frac{\bar{s}}{Q}} + \frac{G_2 \bar{s}}{R^2} e^{-\frac{\bar{s}^2}{2R^2}} + G_3 \bar{s} e^{-\frac{\bar{s}^2}{2}}}{2\sqrt{m_0}}, \tag{9}$$

where $\bar{s} = \frac{s}{2\sqrt{m_0}}$ denotes the normalised stress range. G_1, G_2, G_3, Q and R are empirical distribution weight factors to be determined from the power spectral moments (Dirlik, 1985). The ith spectral moment of a stress time series P_s is given by

$$m_i = \int_0^\infty f^i P_s df, \tag{10}$$

where f is the frequency in Hz. Then, the expected fatigue damage per unit time can be computed by using the following closed-form equation

$$E(d) = \frac{\nu_p \left(2\sqrt{m_0}\right)^m \left[G_1 Q^m \Gamma(1+\nu) + 2^{\frac{m}{2}} \Gamma\left(1+\frac{m}{2}\right)(G_2 |R|^m + G_3)\right]}{C}, \tag{11}$$

herein, ν_p is defined as

$$\nu_p = \sqrt{\frac{m_4}{m_2}}. \tag{12}$$

Finally, the expected amount of fatigue damage D_f accumulated in a duration T can be computed as

$$E(D_f) = T \cdot E(d). \tag{13}$$

Note that this approach was developed for both wide-band and narrow-band Gaussian processes. If the time series is expected to be a narrow-band Gaussian process, the PDF can be described by a Rayleigh distribution. Then, the expected fatigue damage can be written as (Bouyssy et al., 1993; Miles, 1954)

$$E(D_f) = \frac{\nu_0 T}{C}\left(2\sqrt{2}\,\sigma_s\right)^m \Gamma\left(1+\frac{m}{2}\right). \tag{14}$$

where ν_0 and σ_s are to be computed from the spectral moments as

$$\nu_0 = \sqrt{\frac{m_2}{m_0}}. \tag{15}$$

$$\sigma_s = \sqrt{m_0}. \tag{16}$$

3. Structural responses of mooring lines

Figs. 7 and 8 show the maximum mooring tension developed at the fairlead and anchor points, respectively, under the action of homogeneous and inhomogeneous wave loads. As expected, the fairlead points are subjected to an average of 22% higher tensile loads than the anchor points owing to the buoyancy effect of the seawater. However, it appears that the inhomogeneous waves have little effect on the maximum mooring tension. This is due to the fact that the initial pretension in the mooring lines is much larger than the wave-induced mooring loads. A close inspection shows that the pretension contributes more than 90% of the total mooring tension. Nevertheless, the wave load cases LC3.1 and LC4.1 corresponding to the inhomogeneous wave condition 1 generally tend to induce slightly larger tension than the homogeneous wave load case LC1, especially for mooring clusters 1 to 3. This could be explained as being due to the fact that oblique inhomogeneous wave loads lead to higher excitation of the bridge responses (Dai et al., 2020a). On the contrary, the inhomogeneous wave condition 2 (LC3.2 and LC4.2) leads to slightly lower mooring tension as a result of the locally smaller significant wave height H_s and peak period T_p. At the location of mooring cluster 4, all six wave load cases have very similar wave conditions. Consequently, the maximum mooring line tensions are virtually the same for all six wave load cases.

Figs. 9 and 10 plot the standard deviations of tension in the mooring lines, which characterise the dynamic variation due to wave loads. In contrast to the maximum responses shown in Figs. 7 and 8, the difference between the fairlead and anchor points is below 2%, which is negligible. Furthermore, the standard deviations are found to be substantially affected by the inhomogeneities in the wave field. More specifically, the inhomogeneous wave condition 1 induces much higher dynamic responses of the mooring tension, especially for mooring clusters 1 and 2. This could be explained as due to the fact that the inhomogeneous waves considered in LC3.1 and LC4.1 are more oblique (and thus higher excitation forces are acting on pontoons) than homogeneous waves near these two mooring clusters (Dai et al., 2020a). The obliquity of inhomogeneous waves reduces when approaching mooring cluster 4 where it closely resembles a beam sea. Consequently, homogeneous wave loads are found to induce higher standard deviations of the mooring line tension than inhomogeneous wave loads, particularly for the mooring lines at the weather side, i.e. mooring lines 1 to 4. As for the inhomogeneous wave condition 2, all the induced standard deviations of mooring tension are smaller than the homogeneous wave condition, even for mooring cluster 4 where the inhomogeneous wave condition is identical to the homogeneous wave condition. Apparently, the lower H_s and T_p between the bridge south end and the pontoon location A27 also affect the responses of the bridge segment in the vicinity of the bridge north end. The wave correlation is found to have some effects when there is no spatial variation of H_s, T_p and θ_p. For the two inhomogeneous wave conditions, the effect of wave correlation is rather small.

Table 4 lists the standard deviations (SD), mean and maximum (Max) values of the mooring tension at the fairlead point of mooring line 2 in cluster 2 under the inhomogeneous wave load case LC4.1. This point is purposely chosen in view of the fact that the largest tension among all four clusters of mooring lines occur at this particular location. The statistical values computed from each of the five 1-h simulations and their averages are compared with the compiled equivalent 5-h simulation. Note that the equivalent 5-h simulation is a compilation of the data from the five 1-h simulations. As it can be seen, the relative differences due to 1-h simulations are limited, and the use of their averages can effectively reduce the statistical uncertainties.

To further examine the effect of inhomogeneous waves on the mooring line responses, power spectral and wavelet analyses are carried

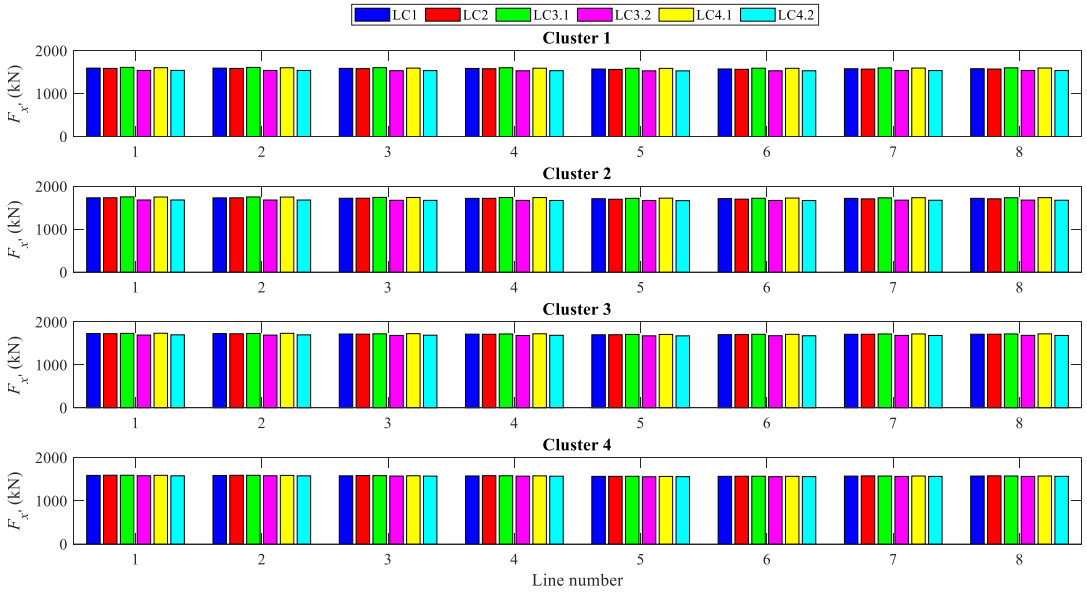

Fig. 7. Maximum mooring line tension at fairlead points.

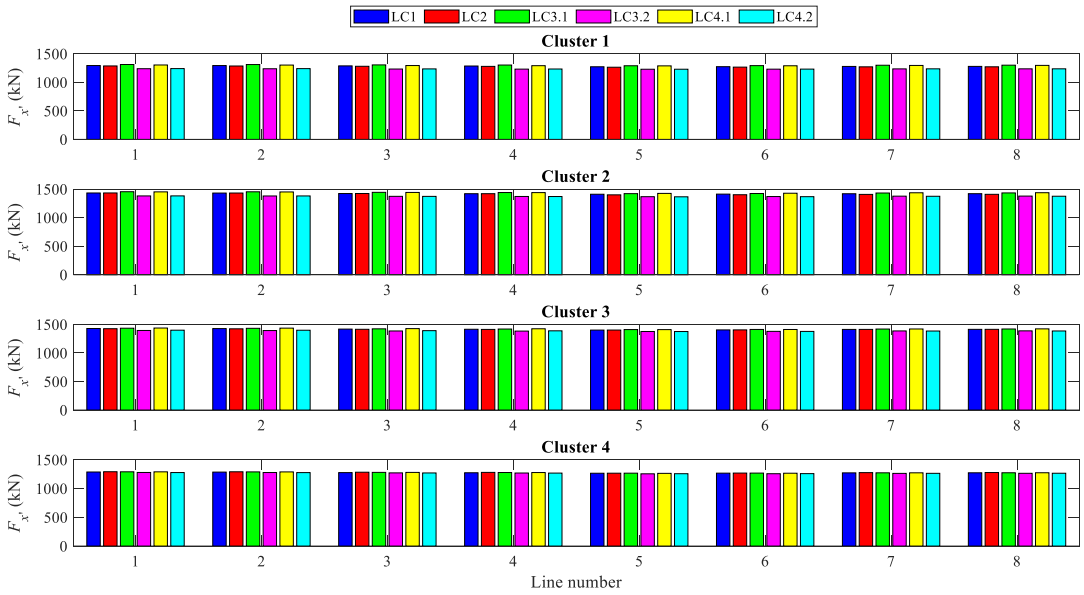

Fig. 8. Maximum mooring line tension at anchor points.

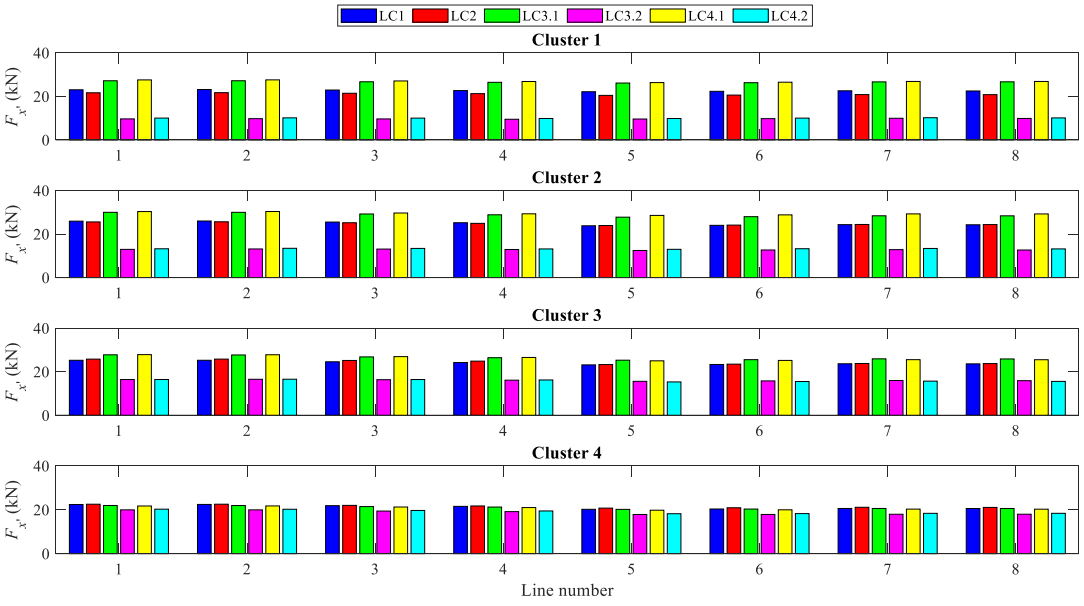

Fig. 9. Standard deviation of mooring line tension at fairlead points.

out with regard to the tension at the fairlead point of mooring line 2 in cluster 2, as shown in Fig. 11. Estimation of the power spectral density (PSD) is conducted by using the Welch method with 8 Hamming windows together with a 50% overlap (Ragan and Manuel, 2007). The time-frequency scalogram presented is for a duration of 1 h. As seen in Fig. 11, most energy of mooring tension is concentrated between 0.15 Hz and 0.23 Hz which is about the wave frequency range. In general, the inhomogeneous wave condition 1 with a spatial variation of the wave parameters H_s and θ_p is found to result in a higher PSD of mooring tension for this frequency range. Accordingly, inhomogeneous load cases LC3.1 and LC4.1 induce larger tension in this mooring line. In contrast, the inhomogeneous wave condition 2 leads to a much lower PSD in general although a slightly higher PSD is observed for the frequency range between 0.3 Hz and 0.35 Hz. The low-frequency second order difference frequency wave load components in a homogeneous wave condition induce higher responses than for inhomogeneous wave conditions near 0.03 Hz. Nevertheless, the energy in the low-frequency range is much lower when compared to the wave-frequency range for all the six wave load cases.

4. Fatigue damage in mooring lines

The structural response analysis of the mooring lines shows that inhomogeneous waves have a substantial effect on the dynamic component of mooring tension despite that the maximum tensile forces virtually remain the same regardless of the wave inhomogeneity. This implies that the inhomogeneous wave conditions could strongly affect the fatigue damage in the mooring lines which should be properly accounted for to ensure a safe and economical design. Therefore, it is important to evaluate the amount of fatigue damage in the mooring lines

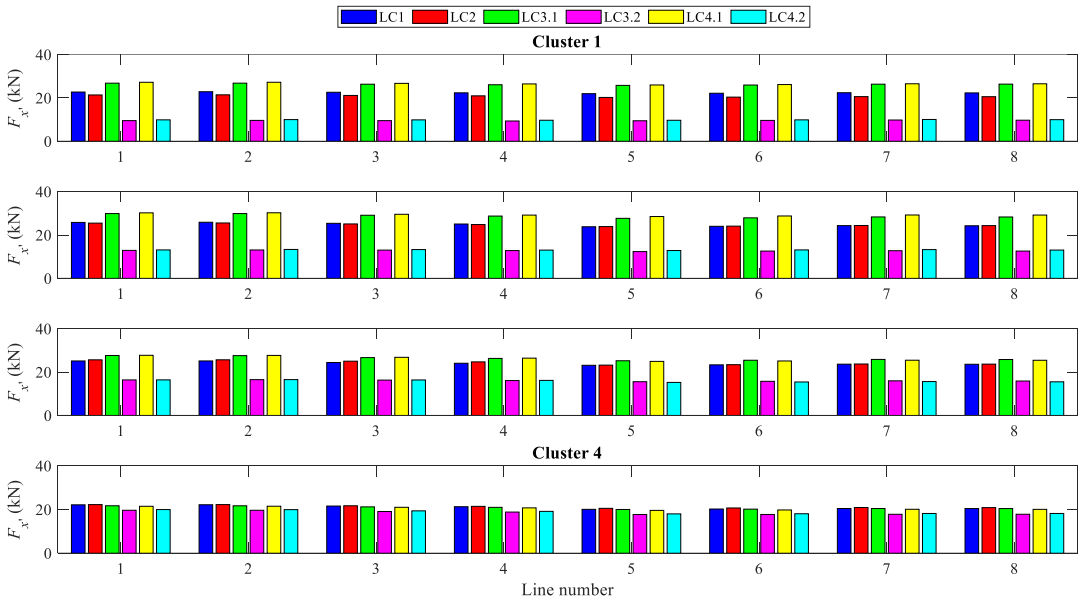

Fig. 10. Standard deviation of mooring line tension at anchor points.

Table 4
Statistical mooring tension at fairlead point of mooring line 2, cluster 2 under LC4.1.

Statistical results		1-h simulation						5-h
		Seed 1	Seed 2	Seed 3	Seed 4	Seed 5	Average	
SD	Value (kN)	30.17	30.16	31.26	30.42	29.68	30.34	30.34
	Difference (%)	−0.58	−0.60	3.02	0.27	−2.18	−0.01	–
Mean	Value (kN)	1634.56	1634.58	1634.60	1634.50	1634.59	1634.57	1634.57
	Difference (%)	0.00	0.00	0.00	0.00	0.00	0.00	–
Max	Value (kN)	1754.91	1754.29	1748.97	1750.88	1736.25	1749.06	1754.91
	Difference (%)	0.00	−0.04	−0.34	−0.23	−1.06	−0.33	–

caused by inhomogeneous waves. It should be highlighted that a typical fatigue analysis includes all possible load cases throughout the service life of the structure under consideration. However, this is not possible for the current study due to the lack of sufficient information on inhomogeneous wave conditions. Still, the response time series for a single sea state may be used for the purpose of solely estimating the effect of inhomogeneous waves on fatigue damage as compared with results for the corresponding homogeneous wave load case. The purpose of this study is thus to obtain an indication of the effect of wave inhomogeneity on fatigue damage based on a limited number of sea states.

Note that the methods for fatigue analysis described in section 2.4, especially the spectral approaches, were developed mainly for Gaussian processes. Therefore, it is important to check the Gaussianity of the mooring tension time series before commencing fatigue damage estimations. Fig. 12 shows the histograms and Gaussian probability plots of the mooring tension at the fairlead point in line 2, cluster 2. In general, the data fit a Gaussian distribution quite well although inhomogeneous wave load cases tend to introduce some nonGaussianities at the tails. Table 5 lists the skewness and kurtosis as well as the Vanmarcke's bandwidth of the data for all six wave load cases. As it can be seen, the skewness is rather small (<0.1 in absolute magnitude) and the kurtosis is very close to 3. The Vanmarcke's bandwidth of the mooring tension due to the inhomogeneous wave condition 2 is slightly higher. This may be because the second order difference-frequency wave components have a relatively higher contribution to the bandwidth as compared to the other wave conditions (see Fig. 11(a)). Nevertheless, the bandwidth is not exceeding 0.25 for all six load cases. Therefore, it may be reasonable to regard the mooring tension time series as a narrow-band Gaussian process. This implies that the analytical approach based on the Rayleigh model by using Eq. (14) may also be appropriate for predicting the fatigue damage in the mooring lines.

For narrow-band Gaussian processes the stress range is known to have a Rayleigh distribution. For wide-band Gaussian processes Dirlik's empirical closed form expression is commonly applied. Both these approaches are used to estimate the fatigue damage together with direct Rainflow cycle counting. In a fatigue damage calculation, the computed mooring tension $F_{x'}$ is first converted to a nominal stress σ_n as

$$\sigma_n = \frac{F_{x'}}{A_n}, \tag{17}$$

where A_n is the nominal cross-sectional area of the mooring line. Note that the nominal diameter of the chain, which is 147 mm as listed in Table 2, also comprises a 20 mm corrosion allowance. For stress calculations, a 50% reduction in the corrosion allowance is accounted for (DNV, 2018a; Multiconsult, 2017). Also note that the effect of mean stress is neglected for the sake of simplicity.

Fig. 13 plots the stress range histogram by using the rainflow cycle counting algorithm for inhomogeneous wave load case LC4.1. Also plotted in this figure is the PDF of the stress range predicted by using Dirlik's method and the classic Rayleigh model. Again, the fairlead point in mooring line 2, cluster 2 is chosen as the point of investigation. As it can be seen, Dirlik's approach is able to approximate the distribution of the histogram based on rainflow counting quite well. The Rayleigh model fails to capture smaller stress ranges when compared with the rainflow cycle counts. Consequently, it tends to slightly overestimate the probability of the occurrence of stress range above 1 MPa. However, stress cycles at low stress ranges may not contribute much to the fatigue

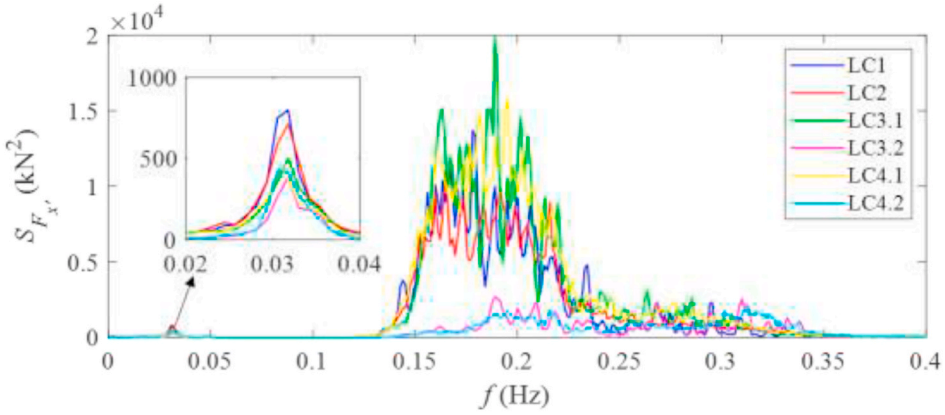

(a)

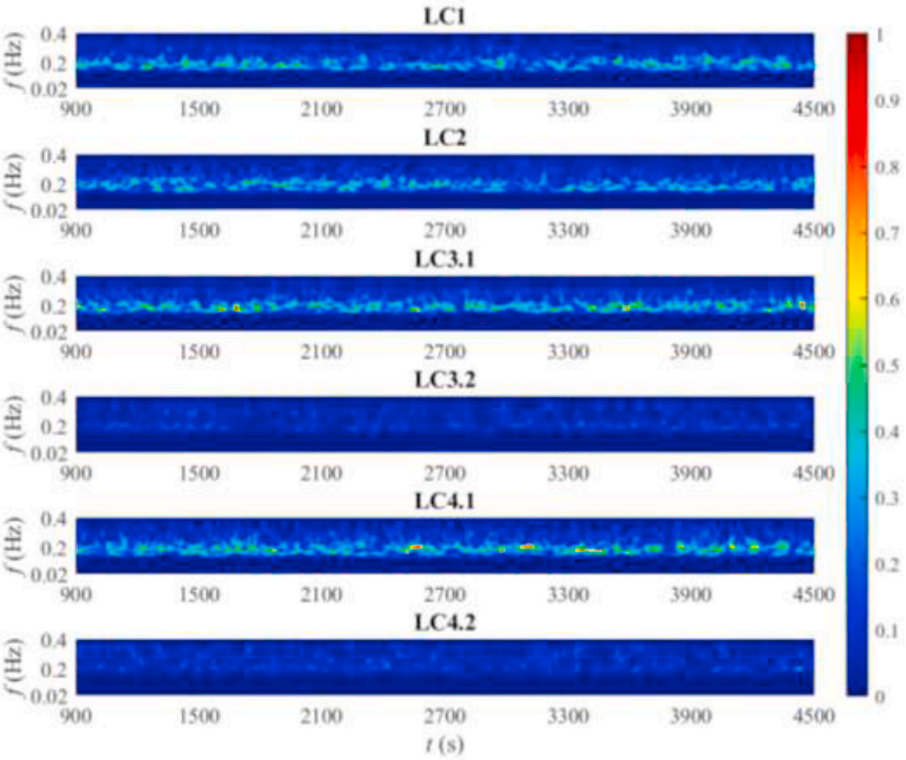

(b)

Fig. 11. Power spectral (a) and normalised wavelet scalogram (b) of mooring tension at the fairlead point in mooring line 2, cluster 2.

damage.

Fig. 14 presents the error of spectral methods in predicting fatigue damage at the fairlead points relative to the results obtained by using the rainflow cycle counting algorithm. In general, the relative error for all load cases studied is found to be less than 6%. Such a small error is commonly deemed acceptable in engineering applications and it implies that both Dirlik's method and the Rayleigh model are able to yield results with a sufficient degree of accuracy. The Rayleigh model based on narrow-band assumption tends to slightly overestimate the fatigue damage. Both methods give predictions with comparable degrees of accuracy, although the error by using the Rayleigh model increases for the inhomogeneous wave condition 2 in which the bandwidth is slightly larger.

Fig. 15 shows the estimated fatigue damage at various critical points of mooring 2 in cluster 2 due to homogeneous and inhomogeneous waves for a duration of 3 h. Note that the fatigue damage is computed by using the direct rainflow cycle counting algorithm. For the chain segments, the fatigue damage at different locations is very similar for all wave load cases. In general, the fairlead point tends to experience the largest fatigue damage. For some load cases, however, it appears that the largest fatigue damage occurs at the top of the bottom segment. This coincides with the finding reported by Xue and Chen (2017) for a similar taut mooring system. The variation of the fatigue damage along the chain segments could be due to the longitudinal drag which tends to reduce the dynamic tension in the mooring lines. For the bottom segment which is close to the seabed, the relative motion between the chain and seawater is expected to be small. Consequently, the drag effect is smaller and the fatigue damage at the top of the bottom segment becomes slightly higher than the anchor point. Nevertheless, the difference in fatigue damage at various locations is very small and may be

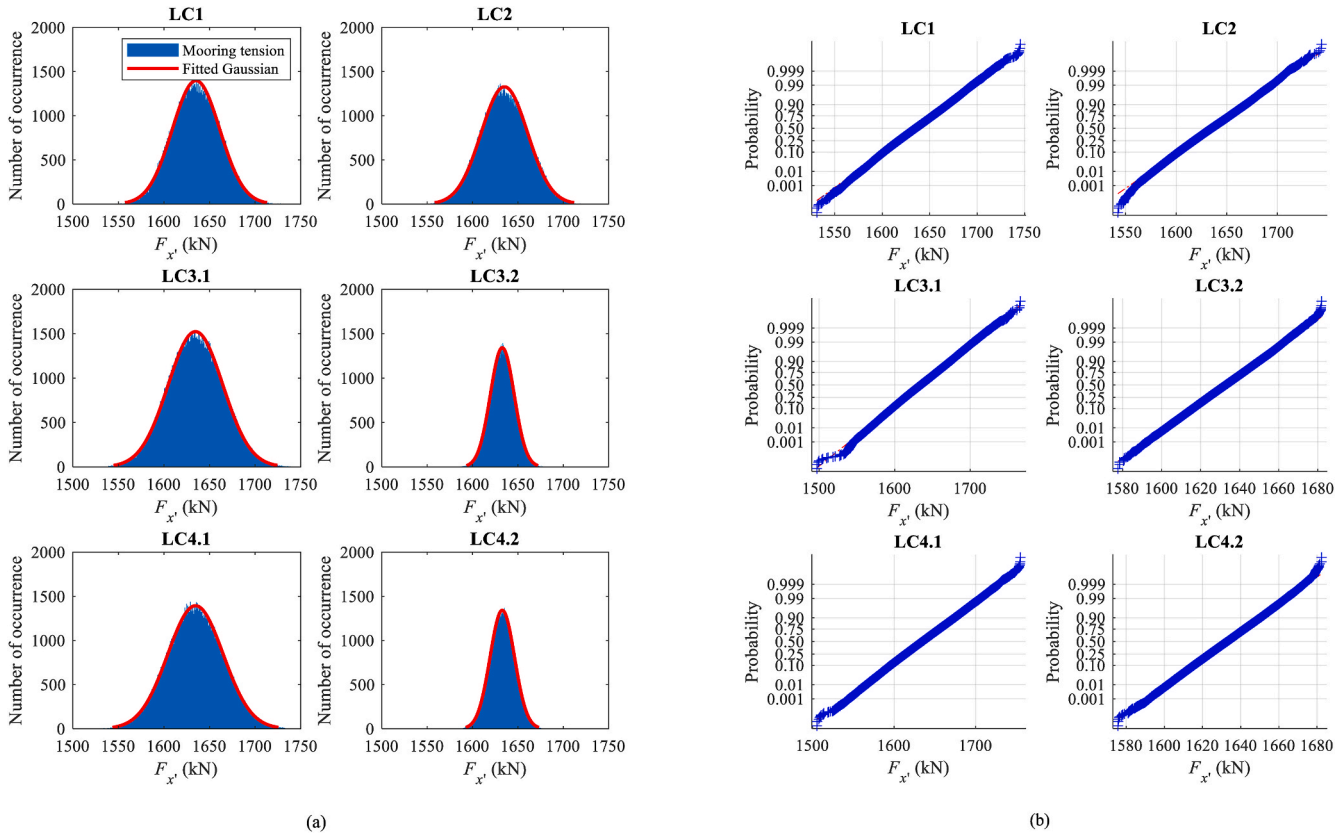

Fig. 12. Gaussianity of mooring tension at fairlead point in line 2, cluster 2: (a) histograms and (b) Gaussian probability plots.

Table 5
Skewness, kurtosis and bandwidth of mooring tension at fairlead point in line 2, cluster 2.

Parameter	LC1	LC2	LC3.1	LC3.2	LC4.1	LC4.2
Skewness	0.05	0.04	0.05	−0.01	0.05	−0.01
Kurtosis	2.84	2.81	2.90	2.90	2.92	2.91
Bandwidth	0.23	0.23	0.22	0.25	0.22	0.25

neglected. For the wire segment, the fatigue damage is much lower than the chain segments. However, due to the lack of long term experience using the wire segments, the possible replacement of all wire segments throughout the service life has been accounted for in the preliminary engineering design (Multiconsult, 2017).

Fig. 16 shows the fatigue damage at the fairlead points of all mooring lines. Note that this figure plots the normalised fatigue damage $\overline{D}_f$ with respect to the maximum $D_f = 1.21 \times 10^{-6}$ which is found to occur at the fairlead point of mooring line 2, cluster 2 for inhomogeneous load case LC4.1. The fatigue damage at other locations along a mooring line may be approximated in conjunction with the results presented in Fig. 15. As it can be seen from Fig. 16 the inhomogeneous wave condition 1 significantly amplifies the fatigue damage in the mooring lines, especially for clusters 1–3 where the obliquity of the waves is large. The maximum increase in the fatigue damage at the fairlead points due to inhomogeneous wave load cases LC3.1 and LC4.1 as compared to LC1 is found to be 80%, 77% and 36% for clusters 1, 2 and 3, respectively. Apparently, the adoption of homogeneous wave conditions to simplify the analysis and design may lead to severe underestimations of the fatigue damage in the mooring lines. However, at the location of mooring cluster 4, the effect of inhomogeneous wave condition 1 on fatigue damage is observed to be quite small due to the fact that both local homogeneous and inhomogeneous waves form a near beam sea condition. The discrepancies are below 9%.

The inhomogeneous wave condition 2 is found to induce much lower fatigue damage for all mooring lines than the homogeneous wave condition. The largest discrepancy of 90% between homogeneous and inhomogeneous wave load cases is observed at mooring line 4 in cluster 1. The discrepancy is reduced when moving toward mooring cluster 4 where the maximum difference is 33%. Under such circumstances, application of homogeneous wave conditions may lead to overly conservative estimations of the fatigue damage in the mooring lines.

It is also found that the correlation of sea states along the length of the floating bridge strongly affects the fatigue damage in the mooring lines when the wave characteristics (H_s, T_p and θ_p) are constant throughout the length of the bridge. The discrepancies are up to 20%. For the inhomogeneous wave conditions 1 and 2, however, this effect reduces to 10% and 17%, respectively. This may be explained as being due to the fact that the inhomogeneity in wave characteristics already introduces some effects similar to uncorrelated waves.

5. Conclusions

In this paper, a computational study of the mooring lines for a floating bridge under the action of wave loads is presented. The bridge considered in the study is a 4.6 km long straight and side-anchored floating pontoon bridge for crossing of the Bjørnafjord. Due to the large span of the crossing and a complex topography, the wave field is inhomogeneous. In the numerical studies, one homogeneous wave condition, typically an annual maximum sea state, and two modified inhomogeneous wave conditions accounting for different spatial variations of wave characteristics (H_s, T_p and θ_p), are considered. For each wave condition, a fully coherent and correlated wave load case and a completely uncorrelated wave load case are established. An analysis of the mooring tension reveals that the time series follows a narrow-band Gaussian distribution quite well.

Time domain simulation results show that the extreme values of the

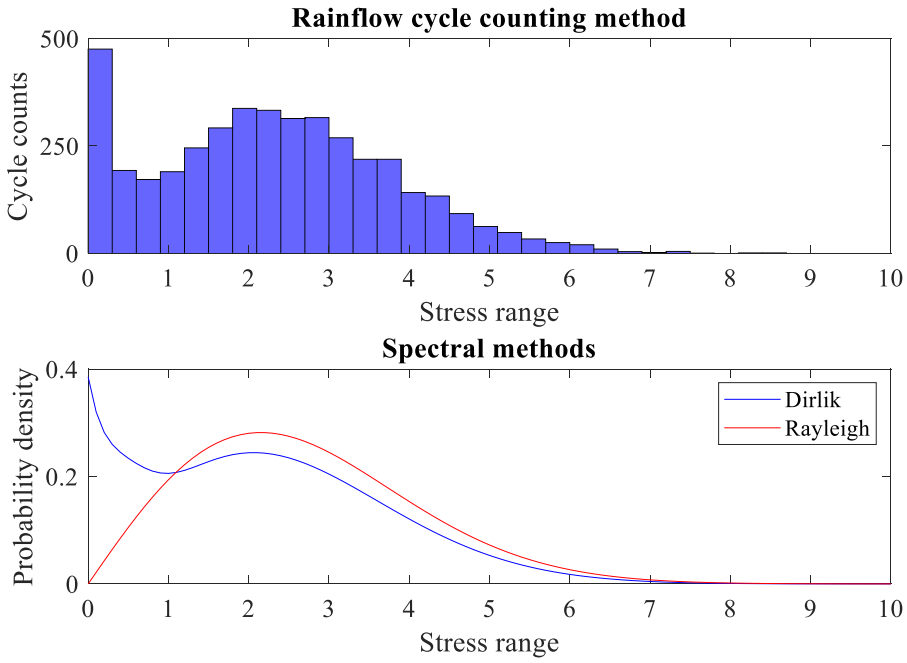

Fig. 13. Comparison of stress range cycle counting at fairlead point in mooring line 2, cluster 2 for inhomogeneous wave load case LC4.1.

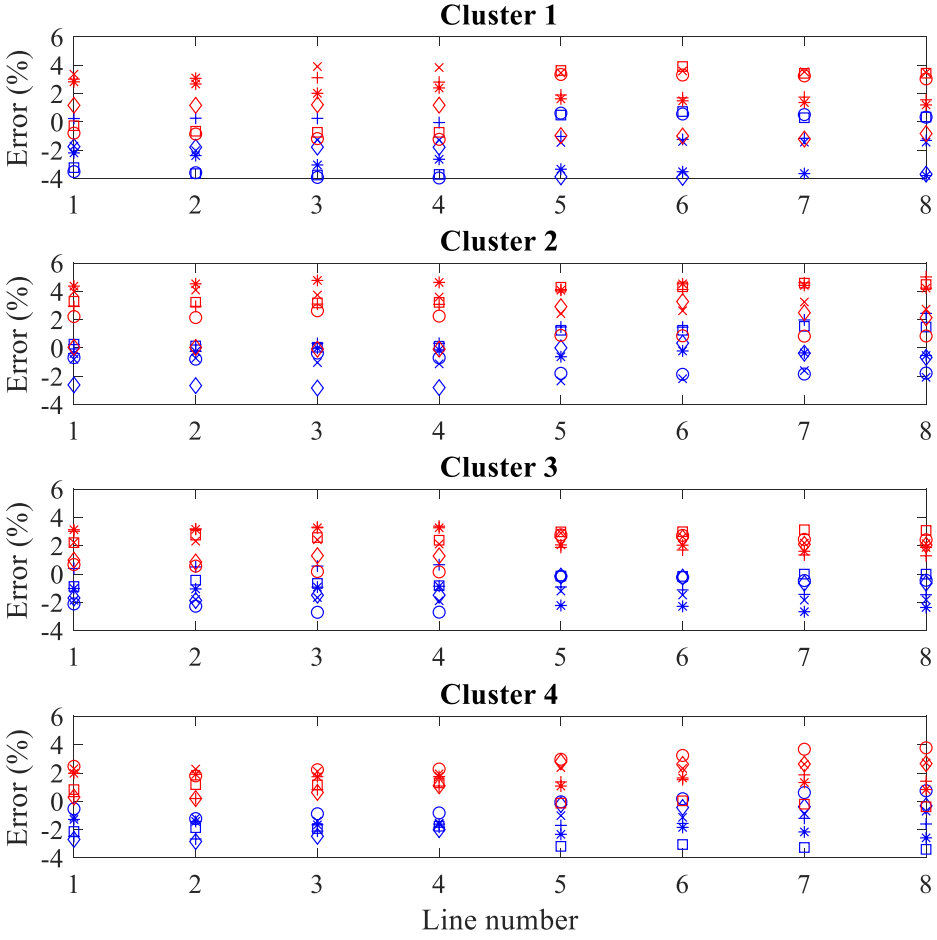

Fig. 14. Error of spectral methods relative to rainflow cycle counting method (○: LC1; □: LC2; ◇: LC3.1; × : LC3.2; +: LC4.1; *: LC4.2; blue markers refer to results by Dirlik's method and red markers are data computed by using Eq. (14)).

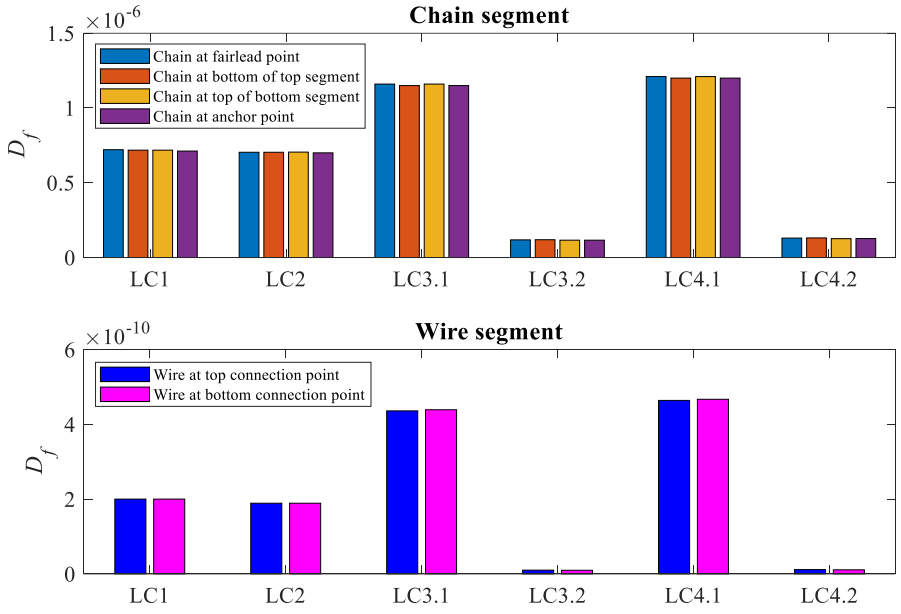

Fig. 15. Fatigue damage in mooring line 2, cluster 2.

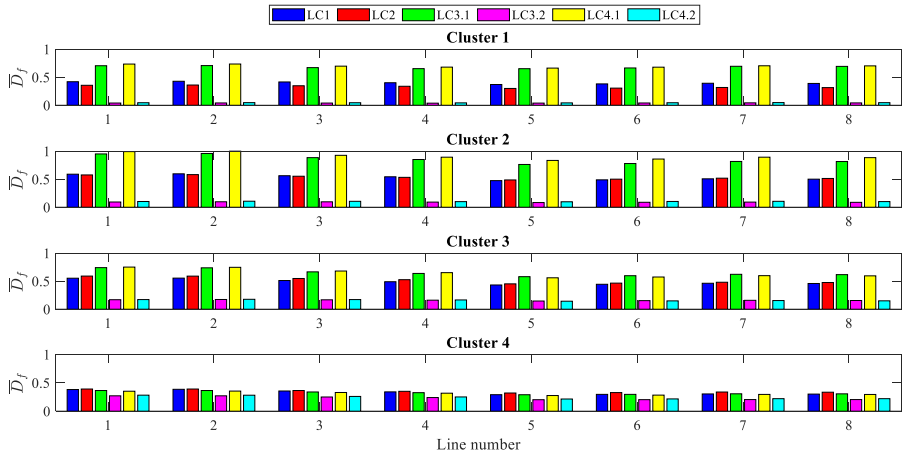

Fig. 16. Normalised fatigue damage in mooring lines at fairlead points.

tension in the mooring lines are mainly governed by the pretension and thus they are virtually unaffected by the inhomogeneity in the wave conditions. However, inhomogeneous wave loads have a considerable effect on the standard deviations of mooring line tension which characterise the dynamic components of the responses, especially for mooring clusters 1–3 where the spatial variation of the wave characteristics is largely different from the homogeneous wave condition.

The fatigue damage of mooring lines due to selected wave load cases is evaluated by using the spectral methods together with the conventional rainflow cycle counting algorithm. A comparison shows that the error associated with Dirlik's method and the Rayleigh model relative to the direct rainflow cycle counting is below 6% for all the six wave load cases that were studied.

Results of short-term fatigue analysis reveal that the spatial variation of wave characteristics (H_s, T_p and θ_p) throughout the entire length of the bridge strongly affect the fatigue damage in the mooring lines. For the two inhomogeneous wave conditions described in the study, the adoption of corresponding homogeneous wave conditions to simplify the analysis and design may lead to either significantly underestimated or overly conservative predictions that would challenge the safety or cost-effectiveness of the design. The correlation of sea states along the length of the floating bridge is also found to affect the fatigue damage in the mooring lines. However, its effect reduces when wave inhomogeneities are present.

Due to the lack of more detailed information related to the wave inhomogeneity, the fatigue analysis presented in this paper is solely for the purpose of obtaining an indication of the inhomogeneous wave effect on the fatigue damage in mooring lines. It should be highlighted that all possible wave conditions throughout the service life of the structure should be taken into consideration as part of a comprehensive fatigue analysis. Therefore, it is highly important that comprehensive numerical simulations or field measurements are conducted such that realistic description and modelling of the inhomogeneous wave conditions are available to achieve a safe and economical design of the mooring systems for very long floating bridges and similar marine structures.

CRediT authorship contribution statement

Jian Dai: Conceptualization, Methodology, Formal analysis, Writing - original draft, Visualization. **Bernt Johan Leira:** Conceptualization,

Writing - review & editing. **Torgeir Moan:** Conceptualization, Writing - review & editing. **Hagbart Skage Alsos:** Resources, Writing - review & editing.

Declaration of competing interest

The authors declare that they have no known competing financial interests or personal relationships that could have appeared to influence the work reported in this paper.

Acknowledgment

This work was supported by the Research Council of Norway through the project 268403/O80 Design and Verification of Large Floating Coastal Structures – Environmental description, structural loads, responses and mooring system.

References

Arany, L., Bhattacharya, S., Macdonald, J., Hogan, S.J., 2014. Accuracy of frequency domain fatigue damage estimation methods for offshore wind turbine support structures. Proceedings of the Second International Conference on Vulnerability and Risk Analysis and Management and the Sixth International Symposium on Uncertainty, Modeling, and Analysis. July, Liverpool, United Kingdom, pp. 13–16.

Benasciutti, D., Tovo, R., 2005. Spectral methods for lifetime prediction under wide-band stationary random process. Int. J. Fatig. 27 (2), 867–877.

Benasciutti, D., Tovo, R., 2006. Comparison of spectral methods for fatigue analysis of broad-band Gaussian random processes. Probabilist. Eng. Mech. 21, 287–299.

Bouyssy, V., Naboishikov, S.M., Rackwitz, R., 1993. Comparison of analytical counting methods for Gaussian processes. Struct. Saf. 12, 35–57.

Calverley, S., 2004. Innovations in Mooring Cable Solutions. Bridon International Ltd, Doncaster, UK.

Chang, A., Li, H., Wang, S., Du, J., 2017. Probabilistic analysis and fatigue damage assessment of offshore mooring system due to non-Gaussian bimodal tension processes. J. Ocean Univ. China 16, 585–601.

Chaudhury, G.K., Dover, W.D., 1985. Fatigue analysis of offshore platforms subject to sea wave loadings. Int. J. Fatig. 7 (1), 13–19.

Chen, L., Basu, B., 2018. Fatigue load estimation of a spar-type floating offshore wind turbine considering wave-current interactions. Int. J. Fatig. 116, 421–428.

Cheng, Z., Gao, Z., Moan, T., 2018a. Hydrodynamic load modeling and analysis of a floating bridge in homogeneous wave conditions. Mar. Struct. 59, 122–141.

Cheng, Z., Gao, Z., Moan, T., 2018b. Wave load effect analysis of a floating bridge in a fjord considering inhomogeneous wave conditions. Eng. Struct. 163, 197–214.

Cheng, Z., Svangstu, R., Gao, Z., Moan, T., 2019a. Field measurements of inhomogeneous wave conditions in Bjørnafjorden. J. Waterw. Port, Coast. Ocean Eng. 145 (1), 05018008.

Cheng, Z., Svangstu, E., Moan, T., Gao, Z., 2019b. Long-term joint distribution of environmental conditions in a Norwegian fjord for design of floating bridges. Ocean. Eng. 191, 106472.

COWI, 2019. Floating Bridge over Bjørnafjord. Retrieved from. https://www.cowi.com/solutions/infrastructure/bjoernafjord-ground-breaking-floating-bridge-for-a-ferry-free-e39-norway. (Accessed 30 December 2019). Accessed.

Cummins, W.E., 1962. The Impulse Response Function and Ship Motions. Report No. DTMB-1661, Washington DC.

Dai, J., Leira, B.J., Moan, T., Kvittem, M.I., 2020a. Inhomogeneous wave load effects on a long, straight and side-anchored floating pontoon bridge. Mar. Struct. 72, 102763.

Dai, J., Abrahamsen, B.C., Leira, B.J., 2020b. Effect of wave-current interaction on structural responses of a very long and side-anchored floating bridge. Proceedings of the 39th International Conference on Ocean. Offshore and Arctic Engineering, USA (in press).

Ding, J., Tian, C., Wu, Y., Wang, X., Liu, X., Zhang, K., 2019. A simplified method to estimate the hydroelastic responses of VLFS in the inhomogeneous waves. Ocean. Eng. 172, 434–445.

Dirlik, T., 1985. Application of Computers in Fatigue Analysis [PhD. Thesis]. University of Warwick.

DNV, G.L., 2018a. SBJ-31-C3-DNV-62-RE-018-0 Bjørnafjorden Side Anchored Floating Bridge - Independent Global Analyses. DNV GL, Oslo, Norway.

DNV, G.L., 2018b. Offshore Standard DNVGL-OS-E301: Position Mooring. DNV GL.

Gao, Z., Moan, T., 2007. Fatigue damage induced by nonGaussian bimodal wave loading in mooring lines. Appl. Ocean Res. 29, 45–54.

Gao, Z., Moan, T., 2008. Frequency-domain fatigue analysis of wide-band stationary Gaussian processes using a trimodal spectral formulation. Int. J. Fatig. 30 (10–11), 1944–1955.

Gao, Z., Moan, T., 2009. Accuracy of the narrow-band approximation of stationary wide-band Gaussian processes for extreme value and fatigue analysis. Proceedings of the 10th International Conference on Structural Safety and Reliability. Japan.

Han, C., Ma, Y., Qu, X., Yang, M., Qin, P., 2016. A practical method for combination of fatigue damage subjected to low-frequency and high-frequency Gaussian random processes. Appl. Ocean Res. 60, 47–60.

Han, C., Ma, Y., Xing, J., Zhang, Z., Liu, K., 2020. An equivalent pseudo spectral method for estimating fatigue damage under two Gaussian random loads. Ocean. Eng. 201, 107072.

Huang, W., Moan, T., 2006. Fatigue under combined high and low frequency loads. Proceedings of the 25th OMAE Conference. Hamburg, Germany.

Jiao, G., Moan, T., 1990. Probabilistic analysis of fatigue due to Gaussian load process. Probabilist. Eng. Mech. 5 (2), 76–83.

Kvåle, K.A., Sigbjörnsson, R., Øiseth, O., 2016. Modelling the stochastic dynamic behaviour of a pontoon bridge: a case study. Comput. Struct. 165, 123–135.

Lei, H., Fu, S., Fylling, I., Fredriksen, A.G., Bonnemaire, B., Kjersem, G.L., 2016. Numerical modelling of floating and submerged bridges subjected to wave, current and wind. Proceedings of the 35th International Conference on Ocean, Offshore and Arctic Engineering. June, Busan, pp. 19–24.

Lotsberg, I., 2005. Background for revision of DNV-RP-C203 fatigue analysis of offshore steel structure. Proceedings of the 24th MOAE Conference (Halkidiki, Greece).

Miles, J.W., 1954. On structural fatigue under random loading. J. Aeronaut. Sci. 21, 753–762.

Multiconsult, 2017. SBJ-31-C3-MUL-22-RE-100-0 – Analysis and Design (Base Case). Multiconsult AS, Oslo, Norway.

Ragan, P., Manuel, L., 2007. Comparing estimates of wind turbine fatigue loads using time-domain and spectral methods. Wind Eng. 31 (2), 83–99.

SINTEF Ocean, 2019a. RIFLEX 4.16.0 Theory Manual, Trondheim, Norway.

SINTEF Ocean, 2019b. SIMO 4.16.0 Theory Manual, Trondheim, Norway.

vegvesen, Statens, 2018. SBJ-32-C3-SVV-90-BA-002 Design Basis Bjørnafjorden Rev E. Statens Vegvesen, Norway.

Van Der Tempel, J., 2006. Design of Support Structures for Offshore Wind Turbines [Ph. D. Thesis]. Delft University of Technology.

Vicinay, 2020. Offshore Mooring Chain Data Sheet. Accessed. https://www.vicinaycadenas.net/mooring-chain/offshore-mooring-chain.asp. (Accessed 9 September 2020). Retrieved from.

Viuff, T., Leira, B.J., Xiang, X., Øiseth, O., 2019. Effects of wave directionality on extreme response for a long end-anchored floating bridge. Appl. Ocean Res. 90, 101843.

Viuff, T., Xiang, X., Leira, B.J., Øiseth, O., 2018. Code-to-code verification of end-anchored floating bridge global analysis. Proceedings of the 37th International Conference on Ocean, Offshore and Arctic Engineering. June, Madrid, Spain, pp. 17–22.

WAMIT, 2019. WAMIT User Manual Version 7.3. Chestnut Hill, USA.

Wei, W., Fu, S., Moan, T., Lu, Z., Deng, S., 2017. A discrete-modules-based frequency domain hydroelasticity method for floating structures in inhomogeneous sea conditions. J. Fluid Struct. 74, 321–339.

Wei, W., Fu, S., Moan, T., Song, C., Ren, T., 2018. A time-domain method for hydroelasticity of very large floating structures in inhomogeneous sea conditions. Mar. Struct. 57, 180–192.

Winterstein, S.R., 1988. Nonlinear vibration models for extremes and fatigue. J. Eng. Mech. 114 (10), 1772–1790.

Xiang, X., Løken, A., 2019. Hydroelastic analysis and validation of an end-anchored floating bridge under wave and current loads. Proceedings of the 38th International Conference on Ocean, Offshore and Arctic Engineering. June, Glasgow, pp. 9–14.

Xiang, X., Viuff, T., Leira, B.J., Øiseth, O., 2018. Impact of hydrodynamic interaction between pontoons on global responses of a long floating bridge under wind waves. In: Proceedings of the 37th International Conference on Ocean, Offshore and Arctic Engineering, Madrid, Spain. June, pp. 17–22.

Xu, T.-J., Zhao, Y.-P., Dong, G.-H., Bi, C.-W., 2014. Fatigue analysis of mooring system for net cage under random loads. Aquacult. Eng. 58, 59–68.

Xue, X., Chen, N., 2017. Palmgren-miner's rule and fracture mechanics based fatigue analysis of deepwater mooring lines. In: Proceedings of the 6th International Conference on Marine Structures, vols. 8–10. May, Lisbon.

Yeter, B., Garbatov, Y., Soares, C.G., 2015. Fatigue damage assessment of fixed offshore wind turbine tripod support structures. Eng. Struct. 101, 518–528.

Yeter, B., Garbatov, Y., Soares, C.G., 2016. Evaluation of fatigue damage model predictions for fixed offshore wind turbine support structures. Int. J. Fatig. 87, 71–80.